# $\bar{K}$-nucleus dynamics: from quasibound states to kaon condensation

Avraham Gal

Racah Institute of Physics, The Hebrew University, Jerusalem 91904, Israel

**Abstract** Coupled-channel $\bar{K}N$ dynamics near threshold and its repercussions in few-body $\bar{K}$-nuclear systems are briefly reviewed, highlighting studies of a $K^-pp$ quasibound state. In heavier nuclei, the extension of mean-field calculations to multi-$\bar{K}$ nuclear and hypernuclear quasibound states is discussed. It is concluded that strangeness in finite self-bound systems is realized through hyperons, with no room for kaon condensation.

**Key words** $\bar{K}N$ dynamics, $\bar{K}$-nuclear quasibound states, kaon condensation

**PACS** 13.75.Jz, 21.45.-v, 21.65.Jk, 21.85.+d, 36.10.Gv

## 1 Introduction

The gross features of low-energy $\bar{K}N$ physics are encapsulated in the leading-order Tomozawa-Weinberg (TW) vector term of the chiral effective Lagrangian [1]. The Born approximation for the $\bar{K}$-nuclear optical potential $V_{\bar{K}}$ due to the TW interaction term yields then a sizable attraction:

$$V_{\bar{K}} = -\frac{3}{8f_\pi^2}\,\rho \sim -55\,\frac{\rho}{\rho_0}\;\;\text{MeV} \qquad (1)$$

for $\rho_0 = 0.16$ fm$^{-3}$, where $f_\pi \sim 93$ MeV is the pseudoscalar meson decay constant. Iterating the TW term plus the less significant NLO terms, within an *in-medium* coupled-channel approach constrained by the $\bar{K}N - \pi\Sigma - \pi\Lambda$ data near the $\bar{K}N$ threshold, roughly doubles this $\bar{K}$-nucleus attraction. A major uncertainty in these chirally based studies arises from fitting the $\Lambda(1405)$ resonance by the imaginary part of the $\pi\Sigma(I=0)$ amplitude calculated within the same coupled channels chiral scheme. However, irrespective of this uncertainty, the $\Lambda(1405)$ which may be viewed as a $K^-p$ quasibound state quickly dissolves in the nuclear medium at low density, so that the repulsive free-space scattering length $a_{K^-p}$, as function of $\rho$, becomes *attractive* well below $\rho_0$. Adding the weakly density dependent $I=1$ attractive scattering length $a_{K^-n}$, the resulting in-medium $\bar{K}N$ isoscalar scattering length $b_0(\rho) = \frac{1}{2}(a_{K^-p}(\rho) + a_{K^-n}(\rho))$ translates into a strongly attractive $V_{\bar{K}}$:

$$\text{Re}V_{\bar{K}}(\rho_0) = -\frac{2\pi}{\mu_{KN}}\text{Re}b_0(\rho_0)\rho_0 \sim -110\;\text{MeV}. \quad (2)$$

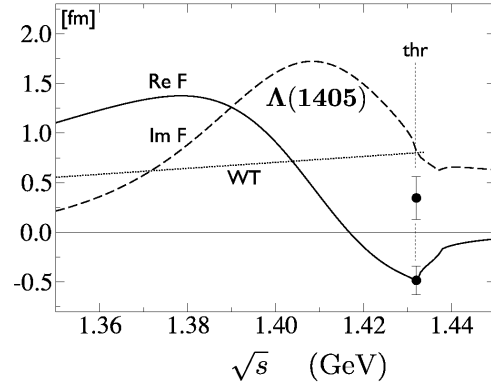The underlying $K^-p$ forward scattering amplitude is shown in Fig. 1.



Fig. 1. The $K^-p$ forward scattering amplitude calculated in the chiral $SU(3)$ coupled channel approach [2]. The scattering length deduced from the DEAR kaonic hydrogen measurement [3] is also shown. The dotted, almost horizontal line indicates the TW amplitude. Figure adapted from Ref. [4].

Comprehensive fits to the strong-interaction shifts and widths of $K^-$-atom levels provide phenomenological evidence for a strongly attractive, and also strongly absorptive $\bar{K}$-nucleus interaction near threshold [5, 6]. These fits yield extremely deep density dependent optical potentials with nuclear-matter depth $-\text{Re}V_{\bar{K}}(\rho_0) \sim (150-200)$ MeV at threshold. Figure 2 illustrates the real part of the best-fit $\bar{K}$-nucleus potential for $^{58}$Ni as obtained for several models. The corresponding values of $\chi^2$ for 65 $K^-$-atom data points are given in parentheses. A model-

independent Fourier-Bessel (FB) fit [7] is also shown, within an error band. Just three terms in the FB series, added to a $t\rho$ potential, suffice to achieve a $\chi^2$ as low as 84 and to make the potential extremely deep, in agreement with the density-dependent best-fit potentials DD and F. In particular, potential F provides by far the best fit ever reported for any global $K^-$-atom data fit [8], and the lowest $\chi^2$ value as reached by the FB method.
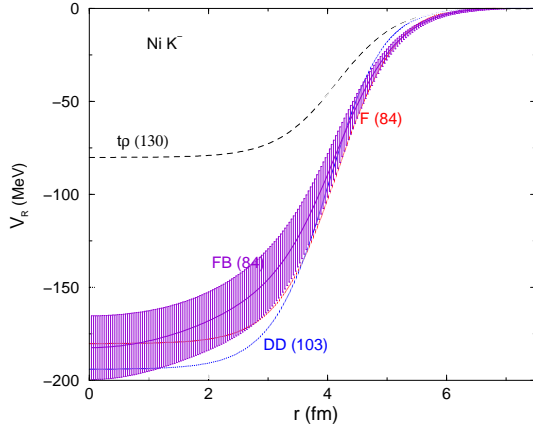


Fig. 2.　Real part of the $\bar{K} - {}^{58}$Ni potential for several density dependent potentials (DD, FB, F) and a $t\rho$ potential fitted to kaonic-atom data [6]. $\chi^2$ values are given in parentheses.
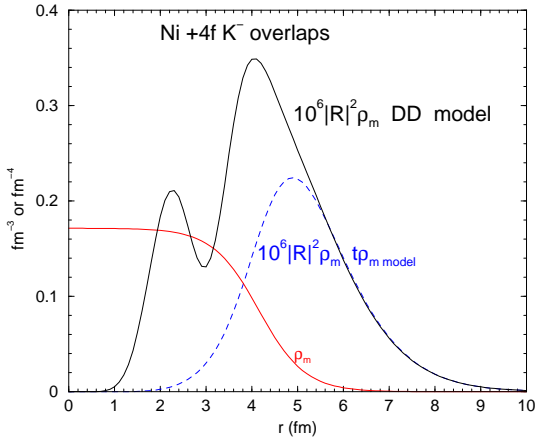


Fig. 3.　Overlaps of $K^-$ $4f$ atomic radial wave-functions $R$ squared with $\rho_m$ of ${}^{58}$Ni, for the $t\rho$ and DD fits of Fig. 2. The nuclear matter density $\rho_m$ is shown for comparison. Figure provided by Eli Friedman.

In Fig. 3 I show the overlap of the $4f$ atomic radial wavefunction squared with the matter density $\rho_m$ in ${}^{58}$Ni for two of the models exhibited in Fig. 2. The $4f$ atomic orbit is the last circular $K^-$ atomic orbit from which the $K^-$ meson undergoes nuclear absorption. The figure demonstrates that, whereas this overlap

for the shallower $t\rho$ potential peaks at nuclear density of order 10% of $\rho_0$, it peaks at about 60% of $\rho_0$ for the deeper DD potential and has a secondary peak well inside the nucleus. The double-peak structure indicates the existence of a $K^-$ strong-interaction $\ell = 3$ quasibound state for the DD potential. It is clear that whereas within the $t\rho$ potential there is no sensitivity to the interior of the nucleus, the opposite holds for the density dependent F potential which accesses regions of full nuclear density. This owes partly to the smaller imaginary part of F.
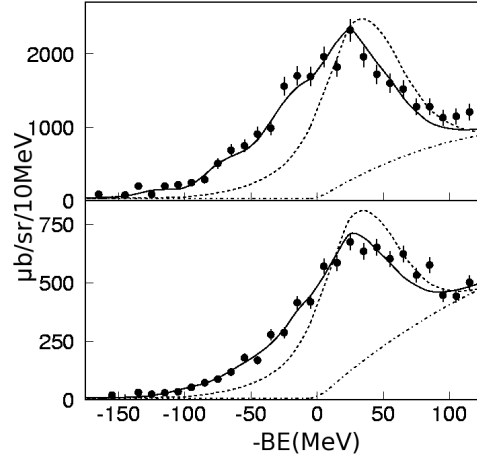


Fig. 4.　KEK-PS E548 missing mass $(K^-, n)$ (upper) & $(K^-, p)$ (lower) spectra on ${}^{12}$C at $p_{K^-} = 1$ GeV/c [9].

A fairly new and independent evidence in favor of extremely deep $\bar{K}$-nucleus potentials is provided by $(K^-, n)$ and $(K^-, p)$ spectra taken at KEK on ${}^{12}$C [9] and very recently also on ${}^{16}$O (presented in PANIC08) at $p_{K^-} = 1$ GeV/c. The ${}^{12}$C spectra are shown in Fig. 4, where the solid lines represent calculations (outlined in Ref. [10]) using potential depths in the range 160-190 MeV. The dashed lines correspond to using relatively shallow potentials of depth about 60 MeV which may be considered excluded by these data. However, Magas *et al.* have recently expressed concerns about protons of reactions other than those *directly* emanating in the $(K^-, p)$ reaction and which could explain part of the bound-state region of the measured spectrum without invoking a very deep $\bar{K}$-nuclear potential [11]. A sufficiently deep potential would allow quasibound states bound by over 100 MeV, for which the major $\bar{K}N \to \pi\Sigma$ decay channel is blocked, resulting in relatively narrow $\bar{K}$-nuclear states. Of course, a fairly sizable extrapolation is involved in this case using an energy-independent potential determined largely near threshold.

A third class, of shallower potentials with $\mathrm{Re}V_{\bar{K}}(\rho_0) \sim -(40\text{-}60)$ MeV, was obtained by imposing a Watson-like self-consistency requirement on the nuclear-medium $\bar{K}N$ $t(\rho)$ matrix that enters the optical potential $V_{\bar{K}} = t(\rho)\rho$ [12, 13]. This is due to the suppressive effect of $\mathrm{Im}t(\rho)$ in the $K^-$ propagator of the Lippmann-Schwinger equation for $t(\rho)$:

$$t(\rho) = v + v \frac{1}{E - H_{\mathrm{mB}}^{(0)} - t(\rho)\rho - V_N + \mathrm{i}0} t \ . \qquad (3)$$

Here $v$ and $t(\rho)$ are coupled-channel meson-baryon (mB) potential and *in-medium t* matrix, respectively, and $H^{(0)}$ is the kinetic energy operator which depends implicitly on the density $\rho$ through the imposition of the Pauli principle in $\bar{K}N$ intermediate states. The $K^-$ optical potential $t(\rho)\rho$ and the nucleon potential $V_N$ act only in $\bar{K}N$ intermediate states. A sizable $\mathrm{Im}t(\rho)$ leads to exponential decay of the propagator $(E - H_{\mathrm{mB}}^{(0)} - t(\rho)\rho - V_N + \mathrm{i}0)^{-1}$, so that $t(\rho) \approx v$ thus losing the cooperative coupling effect to the $\pi Y$ channels in higher-order terms of $v$. However, one needs then to worry about higher orders in the chiral expansion which are not yet in.

I start this review by making brief remarks on the $\bar{K}N - \pi\Sigma$ system, followed by reviewing topics related to $\bar{K}$ nuclear quasibound states: (i) the $K^- pp$ system as a prototype of few-nucleon quasibound states of $\bar{K}$ mesons; and (ii) multi-$\bar{K}$ nucleus quasibound states.
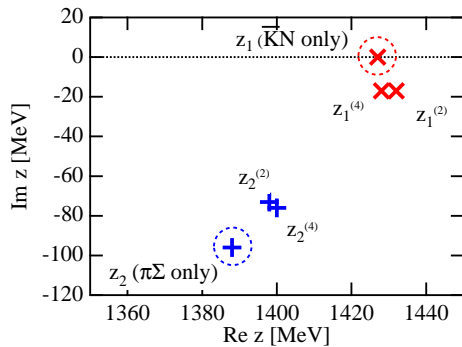
## 2   $\bar{K}N - \pi\Sigma$ coupled channels



Fig. 5.   Pole positions in the complex energy (z) plane of the $\bar{K}N$ ($I = 0$) scattering amplitude resulting from single-channel, two-channel and full (four-channel) models [14].
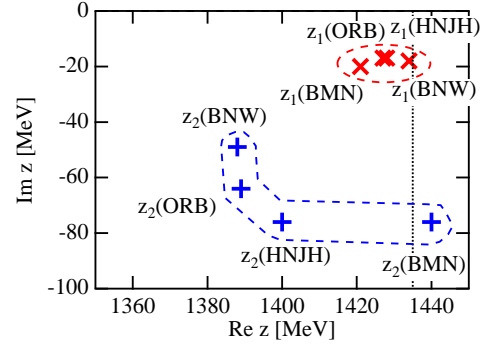


Fig. 6.   Poles of the $\bar{K}N$ ($I = 0$) scattering amplitude in several chiral model applications listed in Ref. [14]. The dotted vertical line denotes the $\bar{K}N$ threshold.

Modern chirally motivated $\bar{K}N - \pi\Sigma$ coupled-channel models give rise to *two* Gamow poles that dominate low-energy $\bar{K}N$ dynamics. Representative pole positions are shown in Fig. 5 and their model dependence is demonstrated in Fig. 6. The $\Lambda(1405)$ resonance, studied in final-state $\pi\Sigma$ interactions, is determined in these models primarily by the lower pole. This identification is further supported, as shown in Fig. 7, by the trajectory of the lower pole which merges into a genuinely $I = 0$ bound state below the $\pi\Sigma$ threshold when the $\bar{K}N$ interaction is sufficiently increased. The upper pole appears in this chiral model [16] above the $\bar{K}N$ threshold. Its position and the trajectory it follows away from the real energy axis make it largely model dependent and sensitive to off-shell effects.
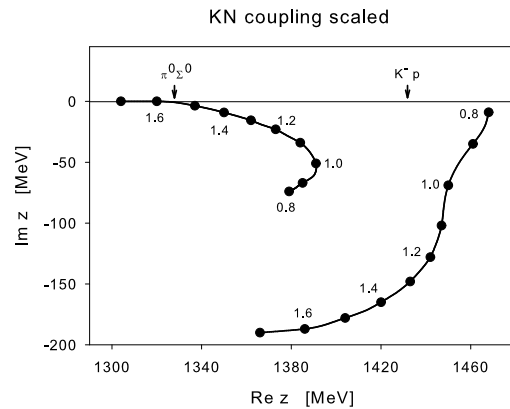


Fig. 7.   Trajectories of Gamow poles in the complex energy (z) plane, on the Riemann sheet $[\Im k_{\bar{K}N}, \Im k_{\pi\Sigma}] = [+, -]$, upon scaling the $\bar{K}N$ interaction strengths [15]. The $\pi^0\Sigma^0$ and $K^- p$ thresholds are marked by arrows.

Surprisingly, however, it is the upper two-body pole that is found to affect significantly three-body $[\bar{K}(NN)_{I=1} - \pi\Sigma N]_{I=1/2}$ coupled channel calculations

for the $K^-pp$ system. The trajectory of the *only* Gamow pole in this system that qualifies for representing a quasibound state is depicted in circles in Fig. 8. Similarly to the trajectory of the $\Lambda(1405)$ in the two-body case, this quasibound $\bar{K}NN$ pole also merges into a genuinely bound state below the $\pi\Sigma N$ threshold which becomes, upon extending the model space, a quasibound $\pi\Sigma N$ state decaying to the $\pi\Lambda N$ and $YN$ lower channels ignored here.
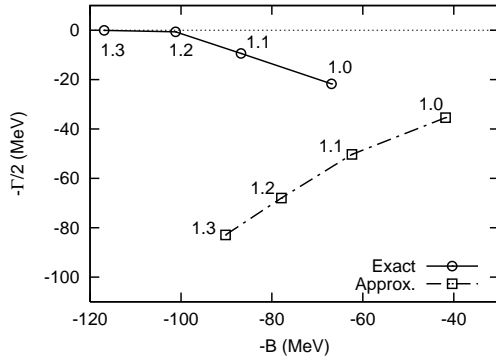


Fig. 8. Variation of $\bar{K}NN(I=1/2)$ quasibound state energy with $\bar{K}N$ interaction strength in three-body coupled-channel (circles) and single-channel (squares) calculations [17].

## 3 Few-nucleon $\bar{K}$ systems

The lightest $\bar{K}$ nuclear configuration maximizing the strongly attractive $I = 0$ $\bar{K}N$ interaction is $[\bar{K}(NN)_{I=1}]_{I=1/2,J^\pi=0^-}$, loosely denoted as $K^-pp$. The FINUDA collaboration presented evidence in $K^-$ stopped reactions on several nuclear targets for

the process $K^-pp \to \Lambda p$, interpreting the observed signal as due to a $K^-pp$ deeply bound state with $(B,\Gamma) \approx (115, 67)$ MeV [18]. However, this interpretation has been challenged in Refs. [8, 19]. A new analysis of DISTO $pp \to K^+\Lambda p$ data claims a $K^-pp$ signal with $(B,\Gamma) \approx (103, 118)$ MeV [20], see Fig. 9. Its location practically on top of the $\pi\Sigma N$ threshold, and particularly the large width, are at odds with any of the few-body calculations listed below, posing a problem for a $K^-pp$ quasibound state interpretation.
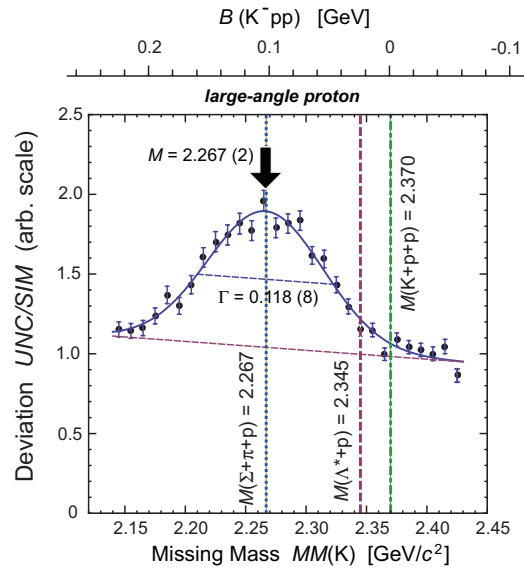


Fig. 9. $K^+$ missing-mass spectrum in the reaction $pp \to K^+\Lambda p$ measured at $T_p = 2.85$ GeV by the DISTO Collaboration [20]. The peak structure with a background (thin line) gives $M = 2267 \pm 2$, $\Gamma = 118 \pm 8$ MeV.

Table 1. Calculated $K^-pp$ binding energies ($B_{K^-pp}$), mesonic ($\Gamma_{\mathrm{m}}$) & nonmesonic ($\Gamma_{\mathrm{nm}}$) widths (in MeV).

| | $\bar{K}NN$ single channel | | $\bar{K}NN-\pi\Sigma N$ coupled channels | | |
| | variational [21, 22] | variational [23] | Faddeev [24] | Faddeev [25] | variational [26] |
|---|---|---|---|---|---|
| $B_{K^-pp}$ | 48 | 17–23 | 50–70 | 60–95 | 40–80 |
| $\Gamma_{\mathrm{m}}$ | 61 | 40–70 | 90–110 | 45–80 | 40–85 |
| $\Gamma_{\mathrm{nm}}$ | 12 | 4–12 | | | $\sim 20$ |

Results of few-body calculations for the $K^-pp$ system are displayed in Table 1. The marked difference between the '$\bar{K}NN$ single channel' binding energies $B_{K^-pp}$ reflects the difference between the input $\bar{K}N$ amplitudes: the YA $I=0$ single-pole amplitude [21] resonates at 1405 MeV, whereas the DHW $I=0$ amplitude [23] resonates at 1420 MeV (close to the upper of two poles). This dependence on the input amplitudes has been verified in a recent coupled-channel Faddeev study [27] and in variational calculations [26].

A notable feature of the $K^-pp$ coupled-channel calculations [24-26] in Table 1 is that the explicit use of the $\pi\Sigma N$ channel adds about $20\pm5$ MeV to the binding energy calculated using effective $\bar{K}N$ potential within a single-channel calculation. This is demonstrated in Fig. 8 by comparing corresponding points on the two trajectories shown there.

Besides present $p(p,K^+)$ measurements [28] at GSI, improving on the DISTO $pp \to K^+\Lambda p$ data, the $K^-pp$ system will be explored at J-PARC in the

$^3$He$(K^-, n)$ and $d(\pi^+, K^+)$ reactions [29].

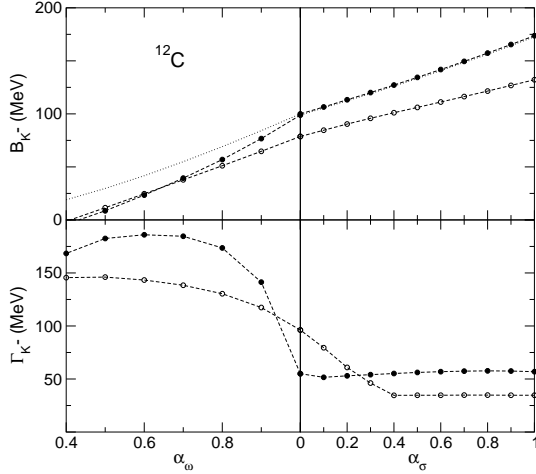## 4  Multi-$\bar{K}$ nucleus quasibound states from RMF calculations



Fig. 10.   $1s$ $K^-$ separation energy $B_{K^-}$ and width $\Gamma_{K^-}$ in $^{12}$C, calculated statically (open circles) and dynamically (solid circles) as a function of the $\omega KK$ and $\sigma KK$ fractional coupling strengths $\alpha_\omega$ and $\alpha_\sigma$, respectively, with $\alpha_\omega$ varied in the left panels as indicated while $\alpha_\sigma = 0$, and with $\alpha_\sigma$ varied in the right panels as indicated while holding $\alpha_\omega = 1$. The dotted line shows $B_{K^-}$ when Im$V_{\bar{K}}$ is switched off in the dynamical RMF calculation [30].

Dynamical relativistic mean field (RMF) calculations of single-$\bar{K}$ quasibound states yield separation energies in the range 100-150 MeV for potentials compatible with $K^-$ atom data [30]. By scanning on the $\omega$ vector-field and $\sigma$ scalar-field strengths, these calculations also provide a quantitative estimate of the width $\Gamma_{K^-}$ as a function of the $K^-$ separation energy $B_{K^-}$. The width comes out larger than 100 MeV near threshold, decreasing to 50 MeV or slightly more as soon as the primary $\bar{K}N \to \pi\Sigma$ decay mode shuts off 100 MeV below threshold [30, 31]. A full systematics for $^{12}$C is shown in Fig. 10 which also demonstrates the substantial gain in $B_{K^-}$ and $\Gamma_{K^-}$ for $B_{K^-} > 100$ MeV when the nuclear core is allowed to adjust dynamically in response to the additional mean field generated by the $\bar{K}$ meson. It is worth noting that the resulting nuclear central densities do not increase by more than a factor 2 with respect to $\rho_0$, and even that is limited to a region of $1-2$ fm about the origin. The figure also shows that Im$V_{\bar{K}}$ may safely be ignored in the calculation of separation energies near and above 100 MeV. These results for $B_{K^-}$ and $\Gamma_{K^-}$, and for nuclear densities, were shown in the RMF cal-

culations of Refs. [30, 31] to hold over a comprehensive range of nuclei from $^{12}$C to $^{208}$Pb.



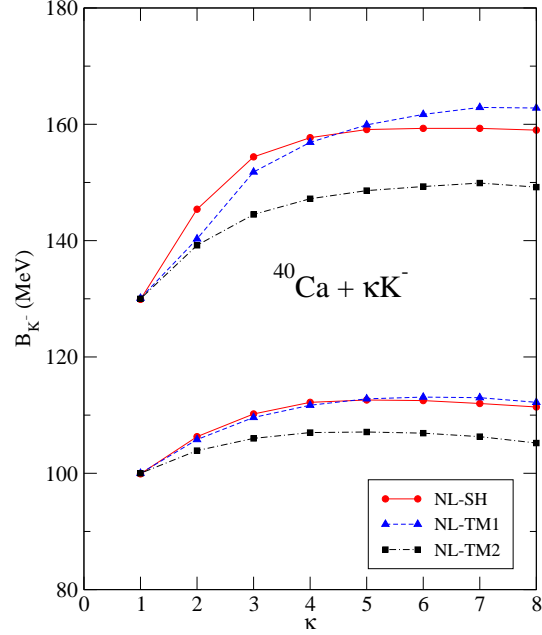Fig. 11.   $K^-$ separation energy $B_{K^-}$, calculated in several nuclear RMF models (see inset) for multi-$K^-$ nuclei $^{40}$Ca$+\kappa K^-_{1s}$. The lower (upper) group of curves was constrained to produce $B_{K^-} = 100$ (130) MeV for $\kappa = 1$ [32].

Highlights of multi-$\bar{K}$ nuclear calculations are summarized below, based on recent work by Gazda *et al.* [32, 33]. In order to establish correspondence with chiral models, particularly with the leading-order TW term, the $\bar{K}$ coupling constants to the vector meson fields were chosen to obey F-type SU(3) symmetry, namely $\alpha_V \equiv F/(F+D) = 1$:

$$2g_{\omega KK} = \sqrt{2}g_{\phi KK} = 2g_{\rho KK} = g_{\rho\pi\pi} = 6.04, \qquad (4)$$

where the value of $g_{\rho\pi\pi}$ is due to the $\rho \to 2\pi$ decay width. The value of $g_{\omega KK}^{\text{SU}(3)} = 3.02$ is lower than any of the other choices made in previous works, as detailed in Ref. [32]. The $\bar{K}$ coupling constant to the scalar field $\sigma$, $g_{\sigma KK}$, was used to fit prescribed values of $B_{K^-}$ in nuclear systems with a single $\bar{K}$ meson. The resulting values of $g_{\sigma KK}$ are also lower than those commonly used, e.g. those inspired by quark models.

$K^-_{1s}$ separation energies $B_{K^-}$ in multi-$K^-$ nuclei $^{40}$Ca$+\kappa K^-$ are shown in Fig. 11 for two choices of $g_{\sigma KK}$, designed within each RMF model to produce $B_{K^-} = 100$ and 130 MeV for $\kappa = 1$. The difference between the various curves, for a given starting value of $B_{K^-}$, originates from the specific balance in each one of these RMF models between the vector fields and the scalar field. A robust saturation of $B_{K^-}$ with $\kappa$ is observed, independently of the applied RMF model, owing to the isoscalar vector-meson fields $(\omega, \phi)$ which

induce repulsion between like $\bar{K}$ mesons. Additional repulsion, in this particular case, is caused by the isovector vector-meson field $\rho$.

The saturation values of $B_{K^-}$ in Fig. 11 are considerably lower than what would be required to convert $\Lambda$ hyperons to $\bar{K}$ mesons through strong decays $\Lambda \to p + K^-$, and also $\Xi^- \to \Lambda + K^-$, in multi-strange hypernuclei which hence remain the lowest-energy configuration for multi-strange systems [34]. This is demonstrated in Fig. 12 for various multi-strange hypernuclei constructed under realistic assumptions on the meson-field couplings to $\Lambda$ and $\Xi$ hyperons [33]. The figure shows little dependence of $B_{K^-}$ on whether or not $\Xi$ hyperons are added to $\Lambda$ hyperons (in a $^{208}$Pb core) and very little dependence (in a $^{90}$Zr core) on the potential depth assumed for $\Xi$ hyperons in nuclei ($V_\Xi^{\mathrm{R}} = -25$ MeV as opposed to the unmarked $V_\Xi^{\mathrm{R}} = -18$ MeV that corresponds relativistically to the nonrelativistic value $V_\Xi^{\mathrm{NR}} = -14$ MeV determined in the BNL-E885 experiment [35]). These RMF calculations across the periodic table provide a powerful argument against $\bar{K}$ condensation under strong-interaction equilibrium conditions in terrestial experimentation. It does not apply, however, to kaon condensation in neutron stars, where equilibrium configurations are determined by weak interactions.
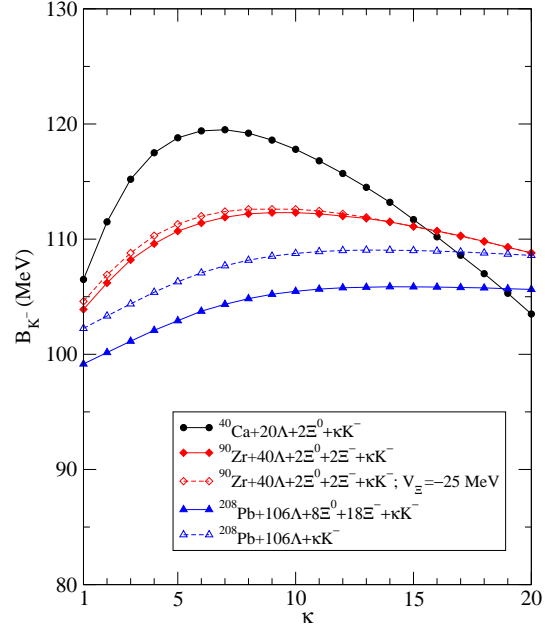


Fig. 12. RMF calculations of multi-$\bar{K}$ quasi-bound states as a function of the number $\kappa$ of $\bar{K}$ mesons in multi-strange nuclei [33].

# References

1　Y. Tomozawa, Nuovo Cimento A **46**, 707 (1966); S. Weinberg, Phys. Rev. Lett. **17**, 616 (1966).

2　B. Borasoy, R. Nißler, W. Weise, Phys. Rev. Lett. **94**, 213401 (2005); Eur. Phys. J. A **25**, 79 (2005).

3　G. Beer, *et al.*, Phys. Rev. Lett. **94**, 212302 (2005).

4　W. Weise, R. Härtle, Nucl. Phys. A **804**, 173 (2008).

5　C.J. Batty, E. Friedman, A. Gal, Phys. Rep. **287**, 385 (1997).

6　E. Friedman, A. Gal, Phys. Rep. **452**, 89 (2007).

7　N. Barnea, E. Friedman, Phys. Rev. C **75**, 022202(R) (2007).

8　J. Mareš, E. Friedman, A. Gal, Nucl. Phys. A **770**, 84 (2006).

9　T. Kishimoto, *et al.*, Prog. Theor. Phys. **118**, 181 (2007); Nucl. Phys. A **827**, 321c (2009).

10　J. Yamagata, H. Nagahiro, S. Hirenzaki, Phys. Rev. C **74**, 014604 (2006).

11　V.K. Magas, J. Yamagata-Sekihara, S. Hirenzaki, E. Oset, A. Ramos, Phys. Rev. C **81**, 024609 (2010).

12　A. Ramos, E. Oset, Nucl. Phys. A **671**, 481 (2000).

13　A. Cieplý, E. Friedman, A. Gal, J. Mareš, Nucl. Phys. A **696**, 173 (2001).

14　T. Hyodo, W. Weise, Phys. Rev. C **77**, 035204 (2008).

15　A. Cieplý, A. Gal, arXiv:0809.0422 (nucl-th).

16　A. Cieplý, J. Smejkal, Eur. Phys. J. A **34**, 237 (2007).

17　Y. Ikeda, T. Sato, Phys. Rev. C **79**, 035201 (2009).

18　M. Agnello, *et al.*, Phys. Rev. Lett. **94**, 212303 (2005).

19　V.K. Magas, E. Oset, A. Ramos, H. Toki, Phys. Rev. C **74**, 025206 (2006).

20　T. Yamazaki, *et al.*, Phys. Rev. Lett. **104**, 132502 (2010).

21　T. Yamazaki, Y. Akaishi, Phys. Lett. B **535**, 70 (2002).

22　Y. Akaishi, T. Yamazaki, Phys. Rev. C **65**, 044005 (2002) [Eq. (29)].

23　A. Doté, T. Hyodo, W. Weise, Nucl. Phys. A **804**, 197 (2008); Phys. Rev. C **79**, 014003 (2009).

24　N.V. Shevchenko, A. Gal, J. Mareš, Phys. Rev. Lett. **98**, 082301 (2007).

25　Y. Ikeda, T. Sato, Phys. Rev. C **76**, 035203 (2007).

26　S. Wycech, A.M. Green, Phys. Rev. C **79**, 014001 (2009).

27　N.V. Shevchenko, A. Gal, J. Mareš, J. Révai, Phys. Rev. C **76**, 044004 (2007).

28　L. Fabbietti (FOPI Collab.), arXiv:0911.0299 (nucl-ex).

29　T. Nagae, Cn. Phys. C **34**, 1259 (2010).

30　J. Mareš, E. Friedman, A. Gal, Phys. Lett. B **606**, 295 (2005); Nucl. Phys. A **770**, 84 (2006).

31　D. Gazda, E. Friedman, A. Gal, J. Mareš, Phys. Rev. C **76**, 055204 (2007).

32　D. Gazda, E. Friedman, A. Gal, J. Mareš, Phys. Rev. C **77**, 045206 (2008).

33　D. Gazda, E. Friedman, A. Gal, J. Mareš, Phys. Rev. C **80**, 035205 (2009).

34　J. Schaffner-Bielich, A. Gal, Phys. Rev. C **62**, 034311 (2000), and references cited therein.

35　P. Khaustov, *et al.*, Phys. Rev. C **61**, 054603 (2000).